TECHNICAL ARTICLE



A Top-Down Characterization of NiTi Single-Crystal Inelastic Properties within Confidence Bounds through Bayesian Inference

P. Honarmandi¹ · M. A. Hossain² · R. Arroyave¹ · T. Baxevanis²

Received: 16 November 2020/Revised: 11 January 2021/Accepted: 22 January 2021 © ASM International 2021, corrected publication 2021

Abstract The inelastic deformation response of NiTi single crystals involves reversible phase transformation and dislocation slip, which is enhanced by the deformation incompatibility among the phases. The phase transformation-plasticity coupling results in decrease in performance, including reduced work output and early fatigue failure. The characterization of the inelastic properties in this material class is crucial for material assessment/ranking and robust performance predictions. Given that direct mesoscale measurements of (coupled) deformation mechanisms are in many cases impractical, top-down characterization of single-crystal properties from limited macroscopic experiments is mostly employed. Here, Bayesian inference and a micromechanics-based continuum single-crystal model are adopted for determining (i) material property values within confidence intervals that allow for a propagation of the quantified uncertainty onto performance predictions, which can be used toward a more efficient design methodology; (ii) ranking of the relative influence of the various material parameters on the deformation response that can further translate to the respective

influence of the various deformation mechanisms conditional on the adopted material model; and (iii) a quantitative evaluation of the importance of the deformation incompatibility among the phases in the overall deformation response.

Keywords NiTi · Materials · Mechanical behavior · Slip · SMA · Stress–strain

Introduction

Deformed Shape Memory Alloys (SMAs) can recover their original shape upon transformation of their crystallographic structure from a low symmetry (martensite) to a higher symmetry (austenite) phase [1-3]. SMAs are, thus, desirable in engineering applications such as vascular stents and monolithic, frictionless, compact, lightweight, solid-state actuators [4-8]. The crystallographic phase transformation is non-diffusive, reversible, triggered by thermal and/or mechanical loading. The martensite phase is formed as thin platelets, needles, or laths within the austenite parent phase, resulting in crystallographic slip, termed TRansformation-Induced Plasticity (TRIP), as a mechanism to accommodate the deformation incompatibility at the austenite-martensite interfaces [9, 10]. TRIP accumulates with transformation cycling, degrading the desired functionality of SMAs and is further responsible for a reduction in transformation stress, strain, and hysteresis [11–18].

Numerous constitutive equations of the deformation response of SMAs at the single-crystal level have been developed based on continuum mechanics [19–31]. These models, which are formulated by incorporating crystallographic information into a local continuum formulation,

M. A. Hossain afzalhossain7.bd@gmail.com

R. Arroyave raymundo.arroyave@tamu.edu

Published online: 01 March 2021



P. Honarmandi hona107@tamu.edu

Department of Materials Science and Engineering, Texas A&M University, College Station, TX 77843, USA

Department of Mechanical Engineering, University of Houston, Houston, TX 77204-4006, USA

allow continuum stresses to be resolved onto individual planes responsible for mediating inelastic deformation. The scale in these models is smeared out and, thus, the spatial arrangement of the crystallographic details is not captured. However, they are (i) easily implementable in numerical methods for the full-field solution of boundary value problems in polycrystalline settings where misorientation across grains, grain boundaries, and triple joints can give rise to complex stress states, and (ii) are amenable to meanfield scale translation rules (e.g., Mori-Tanaka and self-consistent approaches). Due to limitations in simultaneous measuring infinitesimal stress and strain increments at the mesoscale, the constitutive equations are in general derived and calibrated through a top-down approach by fitting material parameters to macroscopic experiments.

Given that material models are abstractions of reality, necessarily simplifying or omitting physical phenomena, assessing the credibility of performance predictions is of critical importance, particularly when these models are used in engineering design. Traditional engineering design is based on empirical safety factors. To allow for more efficient designs, empirical safety factors should be replaced by confidence bounds that account for (i) measurement errors, (ii) deficiencies of the material models used in the material characterization and performance predictions, and (iii) material variability. The growing importance of the related field of Uncertainty Quantification (UQ) is highlighted by the extensive guidelines and standards by the American Society of Mechanical Engineers [32, 33]. UQ methods provide a robust framework for (i) the quantification of uncertainties by handling multiple error sources, (ii) the forward propagation of uncertainty, (iii) model selection in terms of data fit and model simplicity, and (iv) revealing model sensitivities and correlations among model parameters [34–40].

Instead of the classical, deterministic approach to model calibration that yields the single set of material parameter values that best matches the observed data in some appropriate sense, Bayesian inference determines a probability density function (pdf) for the model parameters, i.e., accounts for uncertainty in the estimated parameters. In turn, the model predictions are descriptors of the random field that emerges as a solution of the underlying stochastic model [36, 41-43]. Bayesian inference, rooted in Bayes' theorem, leads to an optimal update on prior knowledge conditional on the observational data. In Bayes' theorem, the likelihood pdf plays a role analogous to the cost/objective function in traditional fitting/optimization describing the error between model predictions and observational data. The error is formulated in terms of either the traditional additive error models [44-46] or embedded error models [47–50]; the latter assigning statistical bias correction terms to the model parameters directly. In the case

of nonlinearity and high-dimensionality, the posterior distribution is evaluated as a stationary distribution of a Markov chain generated by a Markov Chain Monte Carlo (MCMC) method [51, 52], which can be based on adaptive Metropolis-Hastings algorithms [53-55]. Ranking of the influence of the model parameters and their interdependencies on a model's predictions for the sake of model refinement, e.g., reduction of cost and complexity in model optimization problems, or gaining an insight into the physical process described by the model (conditional to the model) can be provided by ANalysis Of VAriance (ANOVA), which is a global variance-based sensitivity analysis [56-59]. Furthermore, Bayesian inference is a powerful approach for model selection among competing models emulating the response of a physical system [60-62], balancing ability to reproduce data with predictiveness and model simplicity [63-65].

In this paper, the Bayesian approach is adopted for the characterization of the inelastic deformation response of NiTi single crystals in a top-down approach from macroscopic experimental data. Uniaxial compressive loading experiments at six different crystallographic directions are utilized for this purpose [66]. The constitutive model accounts for phase transformation and plastic deformation based on micromechanics to accurately reflect the internal stress states that contribute to TRIP. Due to the complexity of the deformation response several simplifying assumptions are necessarily adopted. The presented analysis provides (i) material parameter values within confidence intervals; (ii) ranking the relative influence of the various material parameters on the deformation response; and (iii) a quantitative evaluation of the importance of accounting for the internal stress rise due to the deformation incompatibility among the phases in the overall deformation response. The obtained results offer an insight into the importance of the various deformation mechanisms in the overall deformation response conditional to the adopted model, and allow for a propagation of the quantified uncertainty onto performance predictions, which can be used toward a more efficient design methodology in which empirical safety factors can be replaced with confidence bounds.

The paper is organized as follows. In "Deformation Response of Single NiTi Crystals" section, the NiTi single-crystal deformation mechanisms are briefly reviewed. The constitutive model accounting for those is presented in "Model for the Deformation Response of Single NiTi Crystals" section. An outline of the Bayesian calibration, model selection, and ANOVA is given in "Outline of Bayesian Calibration, Model Selection, and Analysis of Variance" section and the related results in "Results and Discussion" section. A summary of the findings is provided in "Summary" section.



Deformation Response of Single NiTi Crystals

In NiTi, austenite transforms from a cubic B2 crystallographic structure into 12 monoclinic (B19') martensite variants by mechanical loading and/or cooling. The martensite phase forms within the austenite parent phase with the two phases fitting together along planes, called *invariant* or *habit* planes, that remain unchanged, i.e., neither deform nor rotate. These planes/interfaces are between austenite and twins of martensite variants, called *Habit Plane Variants* (HPVs), that comprise of two *Lattice Correspondent Variants* (LCVs). Crystallographic theory predicts 192 HPVs, i.e., 192 possible distinct interfaces between austenite and martensite [67]. Movement of interfaces between HPVs is referred to as HPV *reorientation*, and movement of interfaces between LCVs as *detwinning*.

Plastic deformation in austenite is strongly influenced by $\langle 100 \rangle \{011\}$ and $\langle 101 \rangle \{001\}$ slip modes [68] and, as recently observed, by $\langle 111 \rangle \{110\}$ [69]. TRIP in austenite is observed during phase transformation as a mechanism to accommodate the deformation incompatibility at the austenite–martensite interfaces [9, 10]. The phase transformation–plasticity coupling detrimentally affects performance, reflected in a reduced work output (functional fatigue) and early fatigue failure (structural fatigue) during repeated thermomechanical cycling [9, 70–86]. The plastic deformation in martensite is mainly due to twin activity, 11 possible twinning systems were pointed out by [87], while only one slip system (001) [100] exists due to the low symmetry of the martensite monoclinic crystal structure.

Model for the Deformation Response of Single NiTi Crystals

The adopted single-crystal model accounts for reversible phase transformation from austenite to HPVs, dislocation slipping in the austenite state, and anisotropy in the elastic properties of the two phases, neglecting reorientation of HPVs, detwinning of LCVs, and deformation twinning in martensite [88]. Thus, the model targets pseudoelasticity and shape memory effect for nearly proportional loading within a range that does not allow for considerable martensite plastic deformation or formation of self-accommodated martensite. The interaction between the two phases is described through the Eshelby tensor by regarding the HPVs as ellipsoidal inclusions embedded in the austenite matrix in order to reflect the internal stress states that can activate dislocation slipping, i.e., TRIP, even for applied load levels that wouldn't otherwise [89, 90].

Kinematics

The inelastic deformation of an SMA crystal is defined as an average over a Representative Volume Element (RVE), which should be large enough to include a sizable set of martensite HPVs and slip systems within a single-crystal austenite. It is further assumed that the austenite—martensite formed interfaces are coherent and their motion along with the dislocation motion is rate-independent.

For later use, the volume fraction of martensite corresponding to the α_{th} -HPV system in an RVE is denoted as ξ^{α} , restricted by $0 \leq \xi^{\alpha} \leq 1$. The total volume fraction of martensite in a crystal, $\xi = \sum_{\alpha} \xi^{\alpha}$, must lie in the range $0 \leq \xi^{\alpha} \leq 1$.

Assuming infinitesimal strains, additive decomposition of the total macroscopic strain tensor reads as

$$\boldsymbol{\varepsilon} = \boldsymbol{\varepsilon}^{\mathrm{e}} + \boldsymbol{\varepsilon}^{\mathrm{t}} + \boldsymbol{\varepsilon}^{\mathrm{p}},\tag{1}$$

where ε^e , ε^t , and ε^p stand for the elastic, transformation, and plastic strain tensors, respectively. Thermal strain is an order of magnitude smaller than the transformation strain and is thus not included for simplicity. The thermal expansion of the monoclinic martensite variants is highly anisotropic [91] and its proper implementation in a single-crystal model is not trivial [92].

Transformation Strain

By the rule of mixtures, the transformation strain can be written as

$$\boldsymbol{\varepsilon}^{\mathsf{t}} = \sum_{\alpha=1}^{N_{\mathsf{t}}} \widehat{\boldsymbol{\varepsilon}}_{\mathsf{t}}^{\alpha} \boldsymbol{\xi}^{\alpha},\tag{2}$$

where $\hat{\boldsymbol{\varepsilon}}_{t}^{\alpha} = \frac{1}{2}g_{t}(\boldsymbol{l}^{\alpha} \otimes \boldsymbol{d}^{\alpha} + \boldsymbol{d}^{\alpha} \otimes \boldsymbol{l}^{\alpha})$, \boldsymbol{l}^{α} , \boldsymbol{d}^{α} , and g_{t} are the stress free transformation strain, the habit plane normal, the transformation direction, and the magnitude of transformation, respectively, for each of the N_{t} martensite HPVs, given by crystallography considerations.

The rate of ε^t thus reads as

$$\dot{\varepsilon}^t = \sum_{\alpha=1}^{N_t} \widehat{\boldsymbol{\varepsilon}}_t^{\alpha} \dot{\boldsymbol{\xi}}^{\alpha}. \tag{3}$$

Plastic Strain

The overall plastic strain tensor can be written as

$$\boldsymbol{\varepsilon}^{\mathbf{p}} = (1 - \xi)\boldsymbol{\varepsilon}_{\mathbf{A}}^{\mathbf{p}} + \sum_{\alpha=1}^{N_{\mathbf{t}}} \xi^{\alpha} \boldsymbol{\varepsilon}_{M_{\alpha}}^{\mathbf{p}}, \tag{4}$$



where ε_{A}^{p} and $\varepsilon_{M_{\alpha}}^{p}$ stand for the plastic strain tensors in the regions occupied by austenite and α_{th} -martensite HPV, respectively.

The rate of ε^p is thus given as

$$\dot{\varepsilon}^{p} = (1 - \xi)\dot{\varepsilon}_{A}^{p} + \sum_{\alpha=1}^{N_{t}} \xi^{\alpha} \dot{\varepsilon}_{M_{\alpha}}^{p} - \sum_{\alpha=1}^{N_{t}} \dot{\xi}^{\alpha} \left(\boldsymbol{\varepsilon}_{A}^{p} - \boldsymbol{\varepsilon}_{M_{\alpha}}^{p} \right)
= (1 - \xi) \left[\dot{\varepsilon}^{p}_{A} - \sum_{\alpha=1}^{N_{t}} \frac{\dot{\xi}^{\alpha}}{1 - \xi} \left(\boldsymbol{\varepsilon}_{A}^{p} - \boldsymbol{\varepsilon}_{M_{\alpha}}^{p} \right) \right]
+ \sum_{\alpha=1}^{N_{t}} \xi^{\alpha} \left[\dot{\varepsilon}^{p}_{M_{\alpha}} - \frac{\dot{\xi}^{\alpha}}{\xi^{\alpha}} \left(\boldsymbol{\varepsilon}_{A}^{p} - \boldsymbol{\varepsilon}_{M_{\alpha}}^{p} \right) \right].$$
(5)

The rate of ε^p can moreover be described by crystallographic slip mechanisms in the austenite phase

$$\dot{\varepsilon}^{\mathbf{p}} = (1 - \xi) \sum_{l=1}^{N_{\mathbf{A}}} {}_{\mathbf{A}} \widehat{\boldsymbol{\varepsilon}}_{\mathbf{p}}^{l} \dot{\boldsymbol{\gamma}}_{\mathbf{A}}^{l}, \tag{6}$$

where $_{A}\widehat{\boldsymbol{\varepsilon}}_{p}^{l}=\frac{1}{2}\left(\boldsymbol{q}_{A}^{l}\otimes\boldsymbol{r}_{A}^{l}+\boldsymbol{r}_{A}^{l}\otimes\boldsymbol{q}_{A}^{l}\right)$ is the orientation tensor of the l_{th} -slipping system of austenite, \boldsymbol{q}_{A}^{l} , r_{A}^{l} , $\dot{\gamma}_{A}^{l}$ are the respective shear direction, slip plane normal, and average shearing rate, respectively, and N_{A} denotes the number of slip systems.

Combining (5) and (6), which hold for every $\xi^{\alpha} \in [0,1], \alpha = 1,...,N_t$, yields

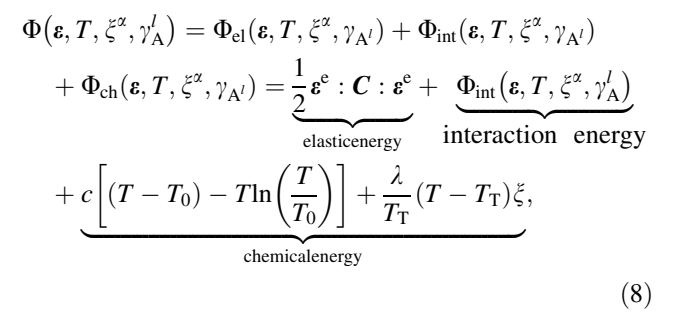
$$\begin{cases} \dot{\varepsilon}_{A}^{p} = \sum_{\alpha=1}^{N_{t}} \frac{\dot{\xi}^{\alpha}}{1 - \xi} \left(\boldsymbol{\varepsilon}_{A}^{p} - \boldsymbol{\varepsilon}_{M_{\alpha}}^{p} \right) + \sum_{l=1}^{N_{A}} {}_{A} \widehat{\boldsymbol{\varepsilon}}_{p}^{l} \dot{\boldsymbol{\gamma}}_{A}^{l}, \\ \dot{\boldsymbol{\varepsilon}}_{M_{\alpha}}^{p} = \frac{\dot{\xi}^{\alpha}}{\xi^{\alpha}} \left(\boldsymbol{\varepsilon}_{A}^{p} - \boldsymbol{\varepsilon}_{M_{\alpha}}^{p} \right). \end{cases}$$
(7)

Thus, the rates of plastic strain in the austenite and α_{th} -martensite HPV are dependent on the dislocation slip rates on austenite's slip systems and on the rates of expansion/shrinkage of the HPVs, thus, the model accounts for the inheritance of plastic strain from one phase to another.

Thermodynamics and Constitutive Equations

Helmholtz Free Energy

Following the choice of the applied strain tensor ε and absolute temperature T as external state variables, the Helmholtz free energy per unit reference volume is taken to be



where the interaction energy is defined through its rate as in [89] ¹

$$\dot{\Phi}_{\text{int}} = (\boldsymbol{C} : \boldsymbol{\varepsilon}^{\text{e}}) : \dot{\boldsymbol{\varepsilon}}^{\text{p}} - \boldsymbol{\sigma}_{\text{A}} : (1 - \xi) \sum_{l=1}^{N_{\text{A}}} {}_{\text{A}} \widehat{\boldsymbol{\varepsilon}}_{\text{p}}^{l} \widehat{\boldsymbol{\gamma}}_{\text{A}}^{l}, \tag{9}$$

and

$$\boldsymbol{\sigma}_{A} = \mathbf{C} : \boldsymbol{\varepsilon}^{e} + \sum_{\alpha=1}^{N_{t}} \xi^{\alpha} \mathbf{C} : (\mathbf{I} - \mathbf{S}^{\alpha}) : \left(\widehat{\boldsymbol{\varepsilon}}_{t}^{\alpha} + \boldsymbol{\varepsilon}_{\mathbf{M}_{\alpha}}^{p} - \boldsymbol{\varepsilon}_{A}^{p}\right),$$

$$(10a)$$

$$\sigma_{\mathbf{M}_{\alpha}} = \sigma_{\mathbf{A}} - \mathbf{C} : (\mathbf{I} - \mathbf{S}^{\alpha}) : (\widehat{\boldsymbol{\epsilon}}_{\mathbf{t}}^{\alpha} + \boldsymbol{\epsilon}_{\mathbf{M}_{\alpha}}^{\mathbf{p}} - \boldsymbol{\epsilon}_{\mathbf{A}}^{\mathbf{p}}).$$
 (10b)

The model parameters \mathbf{C} and c denote the effective stiffness tensor and specific heat at the reference state, respectively. The effective stiffness tensor, C, can be evaluated in terms of the martensite volume fraction, ξ , by the rule of mixtures, i.e., $\mathbf{C}(\xi) = \mathbf{C}_{A} + \xi(\mathbf{C}_{M} - \mathbf{C}_{A}) =$ $C_A + \xi \Delta C$, where the subscripts A and M denote austenite and martensite, respectively. Here, the assumption C = $\mathbf{C}_{\mathrm{M}}^{\alpha} = \mathbf{C}_{\mathrm{A}}$ is adopted for simplicity since first principal calculations show that the elastic properties of the B2 and B19' phases are similar [104]. Moreover, c is assumed to be phase-independent, which is a common engineering assumption. The parameter $T_{\rm T}$ is the phase equilibrium temperature and λ is the latent heat of transformation at temperature $T_{\rm T}$. $\sigma_{\rm A}$ and $\sigma_{\rm M_{\pi}}$ stand for the average stress values in the austenite and the α_{th} -martensite HPV [89], S^{α} stands for the Eshelby's tensor of the α_{th} -martensite HPV, which depends on the elastic constants and shape of the variant, and I is the fourth-order unit tensor.

Using the above expression of the Helmholtz free energy, the standard thermodynamical procedure, commonly referred to as the Coleman–Noll procedure [93], applied to the dissipation inequality



¹ The derivation of the interaction term in [89] is based on the Mori-Tanaka and Kröner micromechanical assumptions and the instantaneous growth hypothesis according to which the martensitic domains form instantaneously.

$$D = \boldsymbol{\sigma} : \dot{\varepsilon} - \dot{\Phi} - \dot{T}s = (\boldsymbol{\sigma} - \mathbf{C} : \varepsilon^{e})$$

$$: \dot{\varepsilon}^{e} + \left(s - c\ln\frac{T}{T_{0}} + \frac{\lambda}{T_{0}}\xi\right)\dot{T}$$

$$+ \sum_{\alpha=1}^{N_{t}} \left[\boldsymbol{\sigma} : \widehat{\varepsilon}_{t}^{\alpha} - \frac{\lambda}{T_{T}(T - T_{T})}\right]\dot{\xi}^{\alpha} + (1 - \xi)\boldsymbol{\sigma}_{A}$$

$$: \sum_{l=1}^{N_{A}} {}_{A}\widehat{\varepsilon}_{p}^{l}\dot{\gamma}_{A}^{l} \ge 0, \tag{11}$$

where s is the entropy, yields the constitutive relationships

$$\boldsymbol{\sigma} = \mathbf{C}(\xi) : \boldsymbol{\varepsilon}^e, \tag{12}$$

$$s = c \ln \frac{T}{T_0} - \frac{\lambda}{T_0} \xi,\tag{13}$$

and reduces the dissipation expression to

$$D = \sum_{\alpha=1}^{N_{t}} \left[\boldsymbol{\sigma} : \widehat{\varepsilon}_{t}^{\alpha} - \frac{\lambda}{T_{T}} (T - T_{T}) \right] \dot{\xi}^{\alpha} + (1 - \xi) \boldsymbol{\sigma}_{A}$$

$$: \sum_{l=1}^{N_{A}} {}_{A} \widehat{\varepsilon}_{p}^{l} \dot{\gamma}_{A}^{l}. \tag{14}$$

Driving Forces

From the above dissipation expression, (14), the driving forces for phase transformation and plastic deformation can be invoked as the quasi-conservative thermodynamic forces conjugate to the respective internal variables.

Martensitic transformation For transformation of austenite to a particular martensite HPV, α , the driving force, F_{α}^{t} , for this HPV should satisfy the following nonequilibrium condition

$$F_{t}^{\alpha} = \boldsymbol{\sigma} : \widehat{\boldsymbol{\varepsilon}}_{t}^{\alpha} - \frac{\lambda}{T_{T}} (T - T_{T}) = {}_{f}f_{t}^{\alpha}, \tag{15}$$

where $_{t}f_{t}^{\alpha}>0$ is the HPV hardness, and $\sigma: \hat{\epsilon}_{t}^{\alpha}$ is the resolved stress on the α_{th} -transformation system, but not in the classical Schmid sense since l^{α} is typically not perpendicular to d^{α} .

For this particular martensite HPV to transform back to austenite, the following condition must be met

$$-F_{t}^{\alpha} = -\boldsymbol{\sigma} : \widehat{\boldsymbol{\varepsilon}}_{t}^{\alpha} + \frac{\lambda}{T_{T}} (T - T_{T}) = {}_{t} f_{t}^{\alpha}, \tag{16}$$

where $_{\mathbf{r}}f_{t}^{\alpha} > 0$.

Plastic deformation of austenite For plastic deformation of austenite, the driving force for dislocation slip of the $l_{\rm th}$ -slip system, ${}_{\rm A}F^l_{\rm p}$, should satisfy the following condition

$$\left|_{\mathbf{A}}F_{\mathbf{p}}^{l}\right| = \left|(1 - \xi)\boldsymbol{\sigma}_{\mathbf{A}} :_{\mathbf{A}}\widehat{\boldsymbol{\varepsilon}}_{\mathbf{p}}^{l}\right| = _{\mathbf{A}}f_{\mathbf{p}}^{l},\tag{17}$$

where $_{A}f_{p}^{l} > 0$ is the respective slip system hardness.

Evolution Equations

The evolution laws of martensitic transformation and plastic deformation are given by the following power–law relations, in which the exponents are chosen sufficiently large to approximate rate-independent conditions.

Martensitic transformation The evolution law for the volume fraction of the α_{th} -martensite HPV follows the power-law relation

$$\dot{\xi}^{\alpha} = \begin{cases} \dot{\xi}_0 \left(\frac{F_t^{\alpha}}{f_t^{\alpha}}\right)^n; & F_t^{\alpha} > 0, \quad \text{austenite} \to \text{martensite} \\ -\dot{\xi}_0 \left(\frac{|F_t^{\alpha}|}{f_t^{\alpha}}\right)^n; & F_t^{\alpha} < 0, \quad \text{martensite} \to \text{austenite} \end{cases}$$
(18)

where

$$\begin{cases}
f_{t}^{\alpha} = \sum_{\beta=1}^{N_{t}} H_{t}^{\alpha\beta} \xi^{\beta} + \xi^{\alpha} J_{t} \gamma + {}_{t}^{c} f_{t}^{\alpha}, \\
f_{t}^{\alpha} = \sum_{\beta=1}^{N_{t}} H_{t}^{\alpha\beta} \xi^{\beta} + (1 - \xi^{\alpha}) J_{t} \gamma + {}_{t}^{c} f_{t}^{\alpha},
\end{cases} (19)$$

where $\dot{\xi}_0$ is a reference transformation strain rate, $\left[H_t^{\alpha\beta}\right]$ is the interaction energy (constant) matrix between the different martensite HPVs, the scalar $J_t>0$ describes the transformation hardening due to plastic deformation, and $\gamma=\sum_{l=1}^{N_A}\left|\gamma_A^l\right|$ is the accumulated total slip. $_{\rm f}^{\rm c}f_{\rm t}^{\alpha}$ and $_{\rm r}^{\rm c}f_{\rm t}^{\alpha}$ are positive scalars.

Plastic deformation of austenite The slip rate in the l_{th} -slip system of austenite is given as

$$\dot{\gamma}_A^l = \dot{\gamma}_0 \left(\frac{{}_{A}F_p^l}{{}_{A}f_p^l} \right) \left(\frac{\left| {}_{A}F_p^l \right|}{{}_{A}f_p^l} \right)^{n-1}, \tag{20}$$

with the evolution law of the hardness, $_{\rm A}f_{\rm p}^l$, reading as

$$Af_{p}^{l} = \sum_{r=1}^{N_{A}} AH_{p}^{lr} |\dot{\gamma}_{A}^{r}|, \quad Af_{p}^{l}(0) = {}_{A}^{c} f_{p}^{l}, \tag{21}$$

where $\dot{\gamma}_0$ is reference plastic strain rate, the matrix

$$_{A}H_{p}^{lr} = {}_{A}H_{p}[q^{l} + (1 - q^{l})\delta_{lr}]\left(1 - \frac{\gamma}{\gamma_{p}^{0}}\right)^{m_{p}},$$
 (22)

describes the history-dependent rate of increase of the deformation resistance on slip system l due to shearing on slip system r, given in terms of the accumulated total slip, q^l stands for a constant latent-hardening parameter that ranges between 1 and 1.04, the positive scalar $_AH_p$ is the initial slip system hardening rate, m_p is the strain hardening exponent, and δ_{lr} are the components of the Kronecker's delta, δ , i.e., $\delta_{lr} = 1$ if l = r and $\delta_{lr} = 0$ if $l \neq r$, $_a^c f_p^l$, $_a H_p$,



Numerical Scheme for the Integration of the Constitutive Response

The numerical procedure adopted for the integration of the constitutive law falls into the class of forward gradient methods, presented in detail in [88] and discussed in [94]. This method leads to improved numerical stability by resulting in a tangent stiffness expression which is considerably reduced from the elastic stiffness; in explicit integration, the maximum allowable time step is inversely related to the relevant material stiffness [95].

The Eshelby tensor is assumed identical for all HPVs and corresponds to oblate spheroids—the martensite phase is formed as thin platelets, needles, or laths within the austenite parent phase—in an isotropic matrix obtained by the isotropization of the stiffness tensor, $\mathbf{C}^{\text{iso}} \equiv (\mathbf{C} :: \mathbf{I}_{\text{V}})\mathbf{I}_{\text{V}} + \frac{1}{5}(\mathbf{C} :: \mathbf{I}_{\text{D}})\mathbf{I}_{\text{D}}$, where $\mathbf{I}_{\text{V}} = \frac{1}{3}\boldsymbol{\delta} \otimes \boldsymbol{\delta}$ and $\mathbf{I}_{\text{D}} = \mathbf{I}_{s} - \mathbf{I}_{\text{V}}$ are the volumetric and deviatoric projection tensors, respectively, \mathbf{I}_{s} designates the fourth-order tensor with components $I_{ijkl}^{s} = \frac{1}{2}\left(\delta_{ik}\delta_{jl} + \delta_{il}\delta_{jk}\right)$, and $\mathbf{A} :: \mathbf{B} = A_{ijkl}B_{lkji}$ for any fourth-order tensors \mathbf{A} and \mathbf{B} . The lengths of the semi-axes of the ellipsoidal HPV inclusions are set as $a_1 = a_2 = a$, $a_3 = a/b$, for b > 1. In the simulations that follow, b is assumed equal to 4.

Outline of Bayesian Calibration, Model Selection, and Analysis of Variance

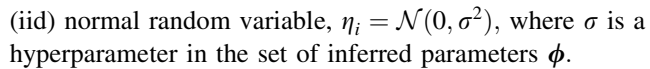
First, the relevant notation and terminology is introduced. Let $M(\mathbf{x}; \boldsymbol{\theta})$ denote the numerical model of an SMA structure with the constitutive response presented in the previous section, which depends on a set of control variables \mathbf{x} (e.g., displacement, temperature), and a set of material parameters $\boldsymbol{\theta}$ to be identified (characterized by a pdf) from a set of reference data \mathbf{d} . The reference data comprises of N data points $\mathbf{d} = [d_i \equiv d(\mathbf{x}_i)]_{i=1...N} \in \mathbb{R}^N$. d_i are the measured values for known control inputs $\mathbf{x}_i \in \mathbb{R}^{q_x}$. The set of parameters characterizing the error terms—i.e., hyperparameters—to be defined below, is denoted by $\boldsymbol{\phi}$. $p(\cdot|\cdot)$ and $p(\cdot)$ denote conditional and marginal pdfs, respectively.

Model for Bayesian Inference

The relation between the measured values d_i and the true process $T(\mathbf{x}_i)$ is represented as

$$d_i = T(\mathbf{x}_i) + \eta_i, \tag{23}$$

where η_i is the measurement error for the i_{th} -observation and is modeled as independent and identically distributed



A strategy to model the relationship between the model output and experimental data is the additive error model [44–46]

$$T(\mathbf{x}_i) = M(\mathbf{x}_i; \, \boldsymbol{\theta}) + \delta(\mathbf{x}_i), \tag{24}$$

where δ is the model discrepancy function that accounts for missing physics in the model (and numerical approximation errors). δ can modeled as a Gaussian process, $\delta(\mathbf{x}_i) = \mathrm{GP}(\mu^\delta(\mathbf{x}_i), C^\delta(\mathbf{x}_i, \mathbf{x}_j))$, with $\mu^\delta(\mathbf{x}_i) = [1, \mathbf{x}_i^T] \boldsymbol{\beta}^\delta = \beta_0^\delta + \beta_1^\delta x_{i,1} + \cdots \beta_{q_x}^\delta x_{i,q_x}$ and $C^\delta(\mathbf{x}_i, \mathbf{x}_{i'}) = \sigma_\delta^2 \frac{2^{1-\nu^\delta}}{\Gamma(\nu^\delta)} \left(\sqrt{2\nu^\delta} Q^\delta\right)^{\nu^\delta}$ (Matérn covariance function), where σ_δ^2 represents the variance of the real process, ν^δ is the smoothness parameter of the covariance function, \mathcal{K}_{ν^δ} is the modified Bessel function of the second kind of order ν^δ ,

 $\Gamma(v^{\delta})$ is the gamma function, and $Q^{\delta}(\mathbf{x}_i, \mathbf{x}_{i'}) = \left[\sum_{k=1}^{q_x} \left(\frac{x_{i,k} - x_{i',k}}{\omega_k^{\delta}}\right)^2\right]^{1/2}$ is the Mahalanobis distance between

 \mathbf{x}_i and $\mathbf{x}_{i'}$ with roughness parameters ω_k^{δ} [96]. The integer part of v^{δ} determines the mean square differentiability of the underlying process. The rest of the parameters $\phi^{\delta} = \left\{\sigma_{\delta}^2, \boldsymbol{\beta}^{\delta}, \boldsymbol{\omega}^{\delta}\right\} \in \boldsymbol{\phi}$, where $\boldsymbol{\beta}^{\delta} = \left[\beta_k^{\delta}\right]_{k=1...q_x}^T$ and $\boldsymbol{\omega}^{\delta} = \left[\omega_k^{\delta}\right]_{k=1...q_x}^T$, are to be inferred from the measurement data.

Note that the discrepancy term δ is not explicitly considered in this paper. As a result, the assumed level of confidence in the simulations ("model = reality") may result in a non-conservative uncertainty reduction.

Bayesian Inference

The Bayes's theorem updates any prior information regarding the parameters θ by incorporating new information obtained from the reference data \mathbf{d} , i.e., combines information from the prior and likelihood pdfs to give a pdf for the parameters

$$p(\boldsymbol{\theta}|\mathbf{d}, M) = \frac{p(\mathbf{d}|\boldsymbol{\theta}, M)p(\boldsymbol{\theta}|M)}{p(\mathbf{d}|M) = \int p(\mathbf{d}|\boldsymbol{\theta}, M)p(\boldsymbol{\theta}|M)d\boldsymbol{\theta}},$$
 (25)

where

- $p(\theta|M)$ is the prior pdf of the parameters;
- $p(\mathbf{d}|\boldsymbol{\theta}, M)$ is the likelihood pdf that plays an analogous role to the cost/objective function in traditional fitting/ optimization in the sense that it describes the discrepancy between model predictions and observational data;



- $p(\theta|\mathbf{d}, M)$ is the posterior pdf that contains all the information on the parameters θ , conditional on \mathbf{d} and M:
- p(d|M) is the evidence pdf, typically ignored when sampling from the posterior since it is a normalizing factor that ensures that the posterior pdf integrates to unity; however, this term plays a central role in model selection, as will be described later.

For simpler notation, M is kept implicit in the following.

Prior Distribution

The prior distribution indicates the initial degree of belief in the parameters' values by either prior quantitative knowledge or subjective expert opinion. It is common practice to assign uninformative prior pdfs to parameters for which little knowledge is available (for example, a uniform distribution or normal distribution with large variances) and assume statistical independence among them

$$p(\boldsymbol{\theta}, \boldsymbol{\phi}) = p(\boldsymbol{\theta})p(\boldsymbol{\phi}). \tag{26}$$

Conjugate priors such that the prior and posterior distributions of the parameter belong to the same family are recommended for practical and computational purposes. Further discussion on the choice of priors may be found in, e.g., [39, 97].

Likelihood

From the statistical models and the above definitions and assumptions, the likelihood function is expressed as a multivariate normal distribution, assuming statistical independence of reference data, as follows

$$p(\mathbf{d}|\boldsymbol{\theta}) \sim \mathcal{N}(\boldsymbol{\mu}, \mathbf{C}),$$
 (27)

where $\mu = [\mathbf{d}_i]_{i=1...N}$, $\mathbf{C} = \sigma^2 \mathbf{I}$, and \mathbf{I} is the $N \times N$ identity matrix.

Posterior Distribution

Given that the model M is nonlinear and multi-dimensional, the posterior pdf $p(\theta|\mathbf{d})$ is evaluated by a Markov Chain Monte Carlo (MCMC) method [51], specifically Gibbs sampler and Metropolis–Hastings (MH) algorithm [53, 54]. The key idea behind MCMC is to generate a Markov chain whose stationary distribution corresponds to the posterior distribution [52]. An adaptive MH algorithm proposed in [98] is used in this work in order to enhance the rates at which the chains generated by the algorithm converge to the posterior distribution. In each iteration of this algorithm, a parameter candidate is sampled from an

adaptive proposal distribution, i.e., a multivariate normal distribution (q), centered at the previous parameter sample in the chain (or the initial guess for the first iteration) with a variance–covariance matrix that is adapted using the variance–covariance of all previous parameter samples in the chain as described by [98]. Then, the parameter candidate is accepted or rejected in a probabilistic manner based on the Metropolis–Hastings ratio

$$MH = \frac{p(\boldsymbol{\theta}^{\text{cand}})p(\mathbf{d}|\boldsymbol{\theta}^{\text{cand}})}{p(\boldsymbol{\theta}^{i-1})p(\mathbf{d}|\boldsymbol{\theta}^{i-1})} \times \frac{q(\boldsymbol{\theta}^{i-1}|\boldsymbol{\theta}^{\text{cand}})}{q(\boldsymbol{\theta}^{\text{cand}}|\boldsymbol{\theta}^{i-1})}, \quad i = \{2, ..., n\}$$
(28)

where the joint densities, i.e., prior \times likelihood, for the sampled candidate, θ^{cand} , and the previous sample in the chain, θ^{i-1} , which are proportional to their posterior densities, are compared using the first ratio, known as the Metropolis ratio. The probabilities of the forward and backward moves from θ^{i-1} to θ^{cand} are also compared using the second ratio (Hastings ratio) in order to account for the asymmetry in the proposal distribution.

At the end, the burn-in period, which that includes the samples before the parameter convergence, is discarded from the sample chain $\{\theta^1...\theta^n\}$. The mean of remaining samples and the square root of diagonal terms in their variance—covariance matrix (standard deviations) indicate the most plausible values and uncertainties of model parameters.

Bayesian Model Selection

Model selection is performed based on the Bayesian hypothesis testing [99]. Assuming all models have equal prior probabilities ahead of analysis, the Bayes factor, i.e., the ratio of marginal likelihoods (or model evidences), is considered as a metric to identify to what extent a model (a null hypothesis) is favored by evidence (data)

$$\mathcal{B}(M_i, M_j) = \frac{p(\mathbf{d}|M_i)}{p(\mathbf{d}|M_j)},\tag{29}$$

where

$$p(\mathbf{d}|M) = \int p(\mathbf{d}|\theta, M)p(\theta|M)d\theta$$
 (30)

is the model evidence. Here, the model selection process involves the pairwise comparison of models, where $\mathcal{B}(M_i, M_j) > 1$ indicates optimality of M_i over M_j and $\mathcal{B}(M_i, M_j) < 1$ the other way around.

Among the different methods proposed to approximate (30) [100], the MCMC sampling from the posterior in an importance sampling-based integration scheme is



adopted, according to which, the model evidence equals a harmonic average of likelihood values

$$p(\mathbf{d}|M_k) \approx \left\{ \frac{1}{n} \sum_{i=1}^n p(\mathbf{d}|\boldsymbol{\theta}_k^i, M_k)^{-1} \right\}^{-1}, \tag{31}$$

associated with the MCMC sampled parameters [60, 100].

ANOVA by Design Of Experiment approach

ANOVA by Design Of Experiment (DOE) is a rigorous technique for global sensitivity analysis that performs well in high-dimensional problems. This approach relies on a set of frequentist hypothesis testing, where the insensitivities of model outcomes to the individual parameters and their interactions are assumed to be the null hypotheses. The model outcome variation (uncertainty) is decomposed into a sum of contributions due to the input factors and their interactions (according to a chosen DoE and appropriate levels for the parameters) to calculate the corresponding F values, i.e., ratios between variances, for ranking the parameters based on their influence on the model outcomes [101, 102]. Herein, a two-level Full-Factorial Design (FFD) is applied to take into account all the level combinations for the parameters, which is equivalent to 2^S level-parameter combinations, where S is the number of parameters.

Results and Discussion

Model Parameter Information

In this section, a summary of the model parameters is given. Those related to the inelastic response are subjected to Bayesian calibration from the experimental data reported in [66] for Ni_{50.9}Ti (at.%) single-crystal isothermal uniaxial loading; deterministic values are adopted for the rest of the parameters. The model parameters are also listed in Table 1a–c. Three dots "…" in the parameter values column indicate that the respective parameters are subjected to probabilistic calibration.

Elastic parameters The B2 structure belongs to the cubic crystal system and thus the elastic tensor of austenite phase in NiTi SMA single crystals possesses three independent constants, i.e., $C_{11}^{A} = 130$ GPa, $C_{22}^{A} = 98$ GPa, and $C_{44}^{A} = 34$ GPa [103]. As already mentioned, the assumption that $\mathbf{C}_{M}^{\alpha} = \mathbf{C}_{A}$ is adopted for simplicity [104].

Transformation parameters Of the 192 possible HPVs predicted by the crystallographic theory of martensite only the 24 Type II-1 HPVs frequently observed in experiments are considered. The components of the vectors \mathbf{l}^{α} and \mathbf{d}^{α} are given in [105, 106] and $g_t = 0.1308$. The interaction

Table 1 Model parameter values

(a) Elastic parameters			
•	Parameter		Value
Austenite	C_{11}^{A} [GPa]		130
	C_{22}^{A} [GPa]		98
	C_{44}^{A} [GPa]		34
HPVs	$\mathbf{C}_{\mathrm{M}}^{\alpha}=\mathbf{C}_{\mathrm{A}}$		
(b) Transformation para	ameters		
Parameter			Value
Equilibrium transformation temperature, T_T , [K]			257
•		2	

Equilibrium transformation temperature, T_T , [K] 257 Latent heat of transformation per unit volume, λ , [MJ/m³] 154 Critical force for forward phase transformation, $_{r}^{c}f_{t}$, [MPa] ... Critical force for reverse phase transformation, $_{r}^{c}f_{t}$, [MPa] ... Hardening coefficient, J_t , [MPa] ...

(c) Austenite plastic deformation parameters

Parameter

Value
Ratio of self to latent-hardening, q^l 1.4

Critical force for slip in $\langle 110 \rangle \{\bar{1}11\}$, ${}^c_{A}f^1_p$, [MPa]

Critical force for slip in $\langle 100 \rangle \{001\}$, ${}^c_{A}f^2_p$, [MPa]

Critical force for slip in $\langle 100 \rangle \{011\}$, ${}^c_{A}f^3_p$, [MPa]

Hardening coefficient, ${}_{A}H_p$, [MPa]

...

The crystallographic data for the 24 martensite HPVs in NiTi is given [105, 106]. The strain rate exponent n is set to n = 50

matrix $\left[H_{\rm t}^{\alpha\beta}\right]$, given in [107], is not accounted for since simulations showed that its inclusion overestimates the transformation hardening observed in the experimental data. The "viscous" parameter n is set to a high value, n=50, to approximate the rate-independent response of NiTi. The reference transformation rate value, $\dot{\xi}_0$, is representative of the applied loading rate, determined using the method suggested in [108].

A deterministic value is adopted for the latent heat, $\lambda = 154 \text{ MJ/m}^3$, calibrated from differential scanning calorimetry [30].

The initial critical forces for forward phase transformation are assumed identical for all martensite HPVs, $_{t}^{c}f_{t}^{\alpha}=_{t}^{c}f_{t}$, and, similarly, $_{r}^{c}f_{t}^{\alpha}=_{r}^{c}f_{t}$. $_{t}^{c}f_{t}$, $_{r}^{c}f_{t}$, and J_{t} are subject to Bayesian calibration.

Parameters related to dislocation slipping— Experimentally, only slip in the system families $\langle 100 \rangle \{001\}$, $\langle 100 \rangle \{011\}$, $\langle 110 \rangle \{111\}$ has been observed [69], and, thus, only these slip families are included in the simulations. The initial critical forces for slip in these systems, ${}^c_A f^l_p$, are assumed identical for each family, and are thus reduced to ${}^c_A f^r_p$ (r=1,2,3). ${}^c_A f^r_p$ (r=1,2,3) and ${}^c_A H_p$ are



evaluated by Bayesian calibration, while the reference plastic strain rate, $\dot{\gamma}_0$, is determined as in [108]. Note that γ_p^0 and m_p in (22) cannot be reliably calibrated from the experiments reported in [66] and are thus assumed null; experiments at a temperature above M_d would be required for their calibration, i.e., a temperature at which stress-induced phase transformation is suppressed.

Probabilistic Model Calibration

The Bayesian inference methodology described in Section 4 is used to perform the probabilistic calibration of the model for the seven parameters, listed in Table 1 with three dots "..." as their values, from the experimental stress-strain curves reported in [66] for Ni_{50.9}Ti (at.%) single crystals uniaxially loaded in six crystallographic directions at room temperature. Since there is no prior knowledge available for these parameters, the prior pdfs are assumed to be uniform over the parameter ranges specified in Table 2. The level of discrepancy between the simulations and experimental data is measured by minimizing the squared Euclidean distance between predicted and experimental stress values, $\Sigma_{\rm pred}^{i,j}$ and $\Sigma_{\rm exp}^{i,j}$, respectively, at specified strain values (denoted by index i) for each loading direction (denoted by index j)

$$\mathbf{D}_{\mathrm{SE}} = \sum_{i} \left(\Sigma_{\mathrm{pred}}^{i,j} - \Sigma_{\mathrm{exp}}^{i,j} \right)^{2},\tag{32}$$

i.e., by minimizing the differences between the predicted and experimental stress-strain curves.

The model calibration is performed by generating 30,000 parameter samples during the MCMC process. After the elimination of the burn-in period, the mean value and standard deviation of the remaining samples for each parameter are calculated and listed in Table 2 as their calibrated value and uncertainty.

Table 2 Initial values, ranges, and MCMC calibrated values with uncertainty for the unknown model parameters

Parameter	Initial value, θ^1	Range, $[\theta_{lb}\theta_{ub}]$	MCMC calibrated value with uncertainty, $\langle \theta \rangle \pm \sigma_{\theta}$
^c _f f _t , [MPa]	2	[1 5]	3.48 ± 1.04
$_{\rm r}^{c}f_{\rm t}$, [MPa]	17	[12 22]	19.95 ± 1.74
$J_{\rm t}$, [MPa]	0.1	[0.001 10]	0.32 ± 0.11
$_{\rm A}^c f_{\rm p}^1$, [MPa]	700	[550 800]	673.36 ± 75.66
$_{\rm A}^{c}f_{\rm p}^{2}$, [MPa]	550	[450 650]	552.31 ± 55.07
$_{A}^{c}f_{p}^{3}$, [MPa]	600	[450 750]	548.40 ± 71.62
$_{A}H_{p}$, [MPa]	0.1	[0.001 10]	3.85 ± 2.84

Uncertainty propagation from the probabilistically calibrated parameters to the model outputs, i.e., the uniaxial stress-strain responses in different loading directions, is performed by running the model for the mean parameter values and each sample in the convergence region, sorting the resulting output samples, and then discarding 2.5% of these samples from the upper and lower bounds to estimate 95% credible intervals. The most plausible model predictions (red lines) and 95% credible intervals (green shaded areas) in addition to the corresponding experimental data (blue lines) are plotted in Fig. 1. Depending on the loading orientation the experimental stress-strain responses differ in terms of the required load level for initiation of forward/ reverse phase transformation, strain hardening, and amount of residual deformation with the simulations to quantitatively reproduce the experimental data in good agreement. The discrepancy between the most plausible model predictions and the experimental data should be attributed to the constitutive model's assumptions/simplifications. mostly to those related to self- and latent-hardening laws due to both phase transformation and plastic deformation and to a lesser extend to others, such as the equal hardness assumption for all HPVs.

Correlations among the parameters is examined via the Pearson correlation coefficient

$$\rho_{X,Y} = \frac{\sigma_{X,Y}}{\sigma_X \sigma_Y},\tag{33}$$

where σ_X , σ_Y , and $\sigma_{X,Y}$ denote the standard deviation of parameter X, the standard deviation of parameter Y, and the covariance between X and Y, respectively, quantifies the linear correlations for each pair of model parameters. The coefficient varies between -1 and 1, where the sign demonstrates the correlation direction. Values closer to -1and 1 imply higher linear correlations between pair parameters, while values closer to 0 correspond to lower correlations. In Table 3, the Pearson correlation coefficients for all pairs of calibrated parameters are tabulated. All coefficient values indicate almost no or weak linear correlations, except for the two hardening parameters, J_t and $_{\rm A}H_{\rm p}$, that show some degree of correlation ($\rho \approx 0.4$). The marginal distributions of J_t and ${}_AH_p$ and their joint (pair) distribution are shown in Fig. 2. Figure 2a and b shows a distinct convergence peak in their marginal frequency distributions, while Fig. 2c and d indicate the convergence region in the joint pdf of these two parameters in 3D and 2D, respectively. Some degree of linearity of color features in Fig. 2d may qualitatively provide the insight indicated from the Pearson correlation coefficient into the linear correlation between the two parameters.



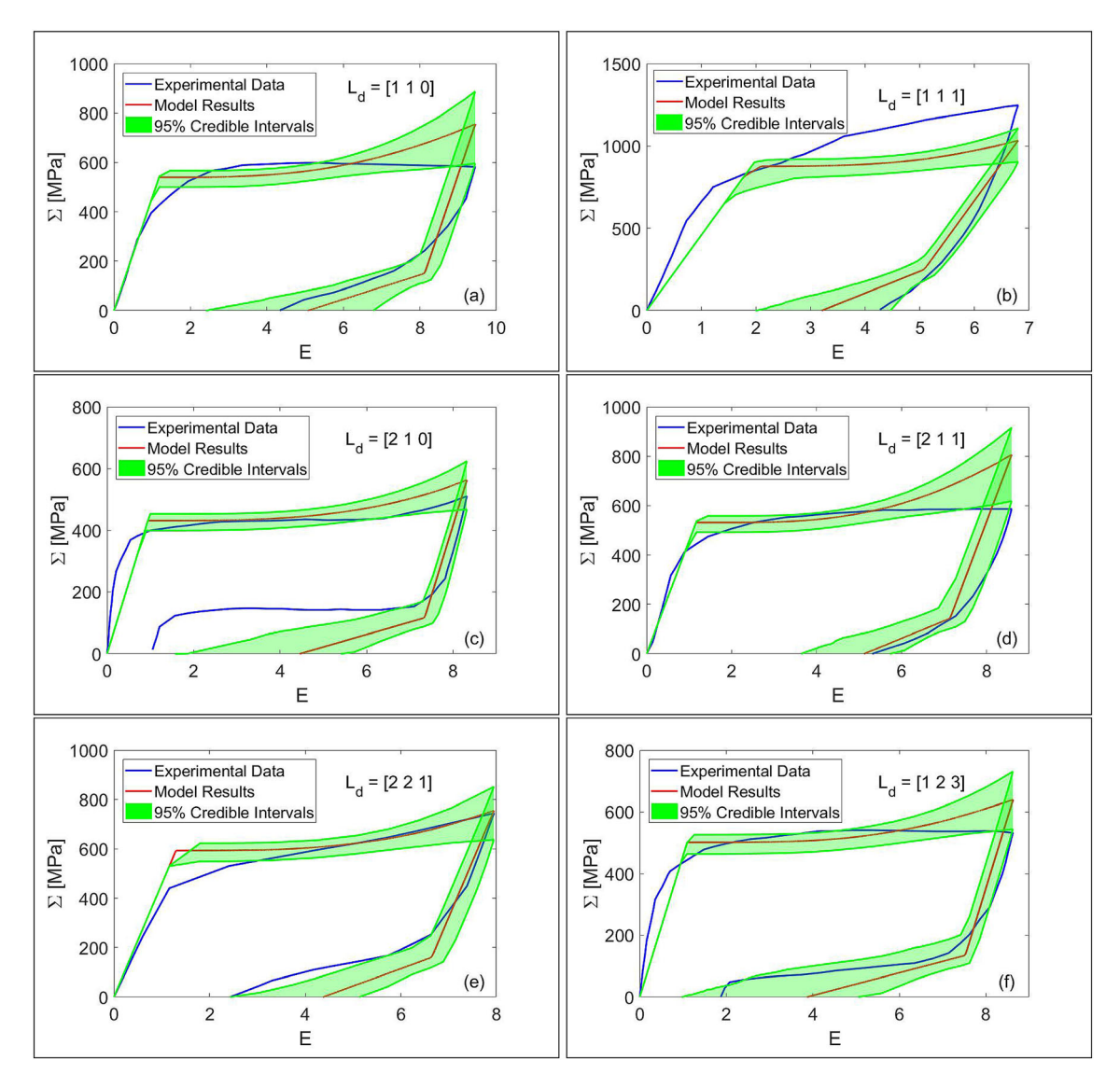


Fig. 1 Experimental stress-strain curves (blue lines) obtained from the uniaxial compressive loading experiments at six crystallographic directions [66], most plausible stress-strain curve predictions (red

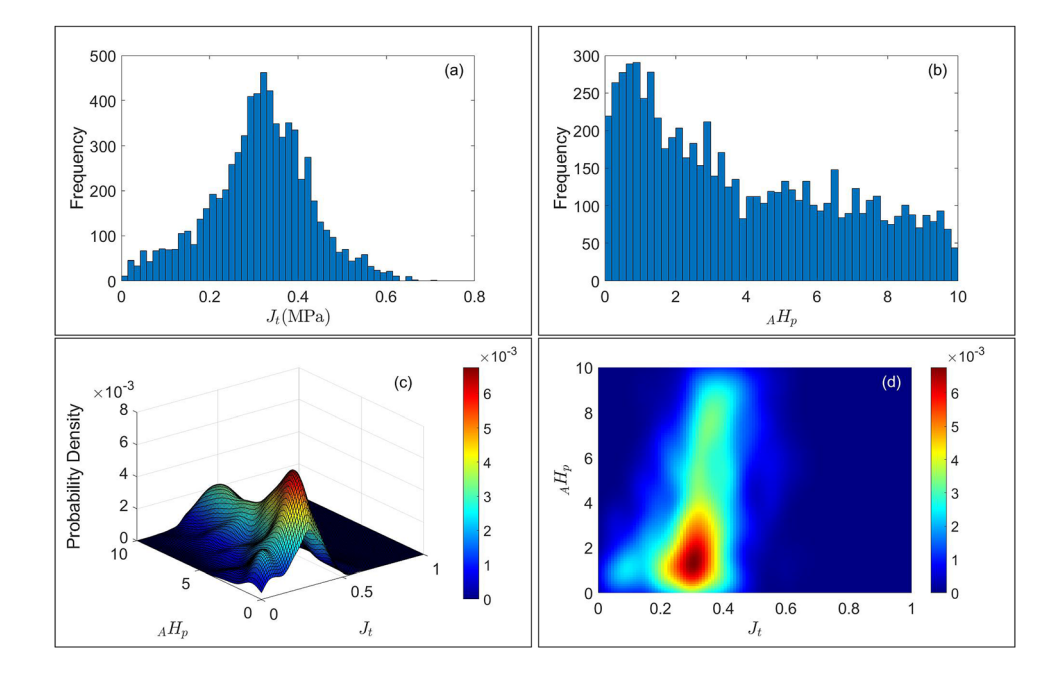
lines), and 95% credible intervals (green shaded areas). For interpretation of the references to color in this figure caption, the reader is referred to the web version of this paper (Color figure online)

Table 3 Pearson correlation coefficients between the pair model parameters

	$_{\mathrm{f}}^{c}f_{\mathrm{t}}$, [MPa]	^c _r f _t , [MPa]	J _t , [MPa]	$_{A}^{c}f_{p}^{1}$, [MPa]	$_{A}^{c}f_{p}^{2}$, [MPa]	$_{A}^{c}f_{p}^{3}$, [MPa]	$_{A}H_{p}$, [MPa]
$_{\rm f}^{c}f_{\rm t}$, [MPa]	1	- 0.05	- 0.29	0.01	- 0.07	0.04	- 0.08
$_{\rm r}^{c}f_{\rm t}$, [MPa]	-0.05	1	0.04	-0.05	- 0.01	- 0.15	-0.27
$J_{\rm t}$, [MPa]	- 0.29	0.04	1	0.21	0.11	-0.001	0.39
$_{A}^{c}f_{p}^{1}$, [MPa]	0.01	- 0.05	0.21	1	0.01	- 0.21	0.06
$_{\rm A}^c f_{\rm p}^2$, [MPa]	-0.07	- 0.01	0.11	0.01	1	-0.08	0.05
$_{\rm A}^{c}f_{\rm p}^{3}$, [MPa]	0.04	- 0.15	- 0.001	- 0.21	-0.08	1	- 0.14
$_{A}H_{p}$, [MPa]	- 0.08	- 0.27	0.39	0.06	0.05	- 0.14	1



Fig. 2 Marginal posterior frequency distribution for parameters J_t and ${}_AH_p$ ((a) and (b) respectively). 3D (c) and 2D (d) joint posterior pdf for the two parameters



Quantitative Analysis of the Contribution of the Inelastic Deformation Mechanisms in Model Performance

As already mentioned, the model accounts for reversible phase transformation from austenite to HPVs and dislocation slipping in the austenite state. In contrast to most existing micromechanics-based single-crystal models, with the exception of [89, 90], a mean-field contribution of the deformation incompatibility at the interphases on the internal stress states that drive dislocation slipping during phase transformation, i.e., TRIP, is introduced. In an effort to elucidate the relative contribution of the inelastic deformation mechanisms and of the aforementioned micromechanical description of the internal stress rise due to the deformation incompatibility among the phases in the overall deformation response, two extra models are constructed and compared pairwise with each other and the adopted model M using the Bayesian model selection outlined in "4.3" section. Model M_A does not account for dislocation slipping and model $M_{\rm B}$ does account for dislocation slipping but without the introduced contribution of the deformation incompatibility among the phases into the driving forces for dislocation slipping, i.e., $\sigma_{\rm A} = \sigma \ (= \sigma_{M_{\pi}})$ in (10).

The probabilistic calibration of M_A and M_B follows the same procedure adopted for M; note that just 3 parameters, ${}^c_{t}f_{t}$, ${}^c_{t}f_{t}$, and J_{t} , need to be calibrated for M_A . The models' outputs for uniaxial loading in the [1 1 1]-direction are compared in Fig. 3. The expected high importance of dislocation slipping in the deformation response is obvious. However, model selection between M_B and M in terms of

model's ability to reproduce data is not possible from a visual comparison alone. The Bayes factor calculated for all pairs of models (Table 4) based on (29) suggest dramatic evidence in favor of models $M_{\rm B}$ and M over model $M_{\rm A}$, in accordance with the visual comparison of the subfigures in Fig. 3, while the evidence in favor of model M over $M_{\rm B}$ is rather weak. M is the most likely model (based on model evidence), with $M_{\rm B}$ being 10% less likely. Thus, the incorporation of the mean-field evaluation of the internal stress that contributes to TRIP does improve the model's ability to reproduce the experimental data and should result in parameter values that are more representative of reality. Note that the calibrated values of the initial critical forces for slip are substantially lower in model $M_{\rm B}$ and the calibrated values of the hardening parameters higher (Table 5).

ANOVA

A two-level FFD-based seven-way ANOVA by DoE is utilized to identify the sensitivity of model outputs to the variations of model parameters listed in Table 2. To perform this analysis, two levels are considered for each parameter based on its 95% credible interval bounds obtained from Table 2, i.e., $\langle \theta \rangle \pm 2 \times \sigma_{\theta}$. The l^2 -norm of squared Euclidean distances (in the form of (32)) between the stress–strain results for the parameter mean values and their counterparts for each level-parameter combination is obtained and input into the ANOVA analysis.

The ANOVA results are shown in Table 6 in descending order for F values that corresponds to a reduction in the parameter influence. Unsurprisingly, the most influential



Fig. 3 Probabilistic model predictions (M_A , M_B , and M) vs experimental stress–strain curve for the uniaxial compressive loading experiment in the [1 1 1]-crystallographic direction

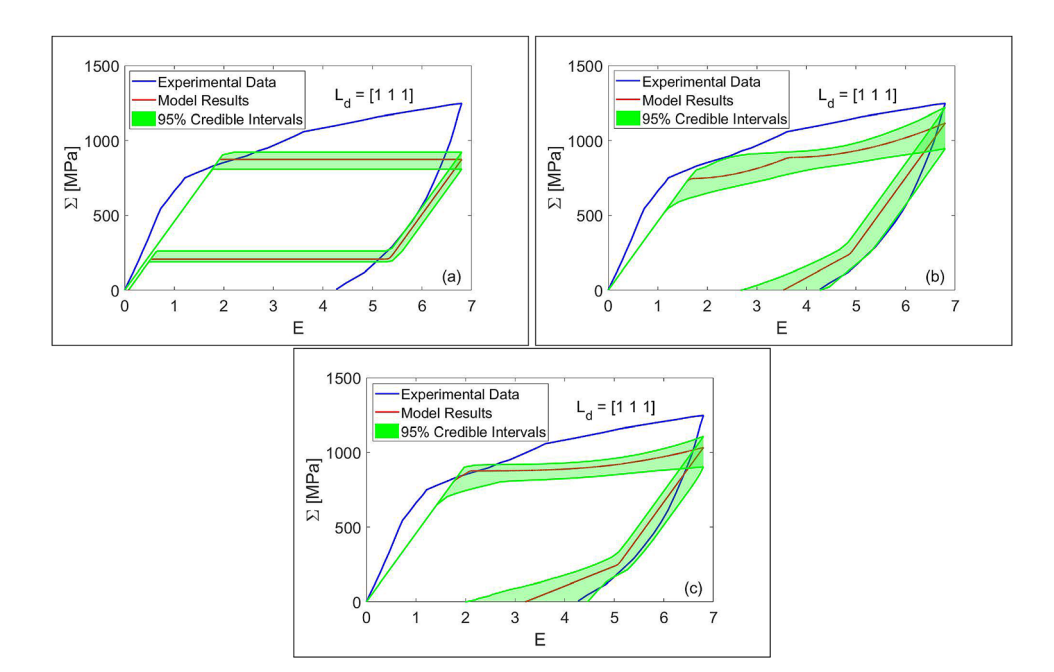


Table 4 Bayes factor, $\mathcal{B}(M_i, M_j)$, for each pair models

M_i	M_j				
	$M_{ m A}$	$M_{ m B}$	M		
$M_{ m A}$	1	2.7×10^{-4}	2.5×10^{-4}		
$M_{ m B}$	3.7×10^{3}	1	0.9		
M	4.0×10^3	1.1	1		

Table 5 MCMC calibrated values of the unknown parameters with uncertainty for models M and $M_{\rm B}$

Parameter	M	$M_{ m B}$
$_{\rm f}^{c}f_{\rm t}$, [MPa]	3.48 ± 1.04	3.77 ± 0.89
$_{\rm r}^{c}f_{\rm t}$, [MPa]	19.95 ± 1.74	20.27 ± 1.37
$_{A}^{c}f_{p}^{1}$, [MPa]	673.36 ± 75.66	498.09 ± 31.80
$_{A}^{c}f_{p}^{2}$, [MPa]	552.31 ± 55.07	469.79 ± 73.88
$_{A}^{c}f_{p}^{3}$, [MPa]	548.40 ± 71.62	537.06 ± 99.56
$J_{\rm t}$, [MPa]	0.32 ± 0.11	0.59 ± 0.24
$_{A}H_{p}$, [MPa]	3.85 ± 2.84	4.90 ± 2.91

parameters are the ones related to the phase transformation, namely, the critical force for forward phase transformation, the transformation hardening due to plastic deformation, and the critical force for reverse phase transformation in a decreasing order of the level of influence on the model outputs.

Table 6 Parameters' information in the FFD-based ANOVA and influence in descending order

	F value
$_{\rm f}^{c}f_{\rm t}$, [MPa]	36.85
$J_{\rm t}$, [MPa]	9.48
$_{\rm r}^{c}f_{\rm t}$, [MPa]	7.76
$_{\rm A}^{c}f_{\rm p}^{\rm l}$, [MPa]	6.09
$_{\rm A}^{c}f_{\rm p}^{3}$, [MPa]	5.05
$_{A}H_{p}$, [MPa]	0.38
$_{A}^{c}f_{p}^{2}$, [MPa]	2.81×10^{-4}

Based on energetic grounds [69], $\langle 100 \rangle \{011\}$ has the lowest energy barrier (the unstable peak value) and hence is most likely to be activated, $\langle 110 \rangle \{\bar{1}11\}$ is a harder slip system, and $\langle 100 \rangle \{001\}$ is the hardest slip system to activate and it has hardly been observed. $\langle 100 \rangle \{011\}$ permits glide only in three independent slip systems out of the six physically possible (or geometric) slip systems, thus $\langle 100 \rangle \{011\}$ cannot produce five independent slip systems to satisfy the Mises criteria for arbitrary deformations, same as $\langle 100 \rangle \{001\}$. $\langle 110 \rangle \{\bar{1}11\}$ can produce five independent slip systems (out of physically possible 12 slip systems). According to the ANOVA by DoE analysis, the ranking of the critical forces for dislocation slipping from the most influential to the least is as follows: $\langle 110 \rangle \{\bar{1}11\}, \langle 100 \rangle \{011\}, \text{ and } \langle 100 \rangle \{001\}.$ The difference in F values between $\langle 110 \rangle \{\bar{1}11\}, \langle 100 \rangle \{011\}$ is quite small and both values are orders of magnitude greater than the F value corresponding to $\langle 100 \rangle \{001\}$, which is a small value ($\ll 1$), i.e., the influence of the $\langle 100 \rangle \{001\}$ on the overall deformation response is negligible.



Summary

Bayesian inference has been employed in order to obtain a quantitative insight into the inelastic deformation response of NiTi single crystals from a limited set of macroscopic uniaxial loading experiments via a phenomenological constitutive response, which is formulated by incorporating crystallographic information into a local continuum formulation. The model accounts for reversible phase transformation from austenite to HPVs, dislocation slipping in the austenite state, and anisotropy in the elastic properties of the two phases, which are considered to be the dominant deformation mechanisms active during the experiments. Using the classical additive error model, a probabilistic calibration of model parameter values is carried out and their mean values and uncertainty are obtained. The Bayesian methodology is appropriate for forward propagation of quantified uncertainty onto performance predictions. Through Bayesian model selection and Analysis of Variance by Design Of Experiment approach, (i) a ranking of the inelastic deformation mechanisms in terms of their relative influence on the overall deformation response, and (ii) a quantitative evaluation of the importance of the nucleation and build-up of slip in austenite to accommodate the high transformation strains upon traversing austenite-martensite interphases, are provided, conditional on the adopted constitutive response.

Acknowledgements PH and RA acknowledge the support of NSF through Grant No. 1849085, as well as Texas A&M University through their X-Grants program. MAH and TB acknowledge the support of NSF through Grant No. CMMI-1917441.

References

- Otsuka K, Wayman CM (eds) (1999) Shape memory materials. Cambridge University Press, Cambridge
- Duerig T, Melton K, Stockel D, Wayman C (eds) (1990)
 Engineering aspects of shape memory alloys. Butterworth-Heinemann, London
- Lagoudas DC (ed) (2008) Shape memory alloys: modelling and engineering applications. Springer, New York
- Hartl DJ, Lagoudas DC (2007) Aerospace applications of shape memory alloys. Proc Inst Mech Eng Part G J Aerosp Eng 221(4):535–552
- Sreekumar M, Nagarajan T, Singaperumal M, Zoppi M, Molfino R (2007) Critical review of current trends in shape memory alloy actuators for intelligent robots. Ind Robot 34(4):285–294
- Nespoli A, Besseghini S, Pittaccio S, Villa E, Viscuso S (2010)
 The high potential of shape memory alloys in developing miniature mechanical devices: a review on shape memory alloy mini-actuators. Sensors Actuators A Phys 158(1):149–160
- Jani JM, Leary M, Subic A, Gibson MA (2014) A review of shape memory alloy research, applications and opportunities. Mater Des 1980–2015(56):1078–1113

- Barbarino S, Flores EIS, Ajaj RM, Dayyani I, Friswell MI (2014) A review on shape memory alloys with applications to morphing aircraft. Smart Mater Struct 23(6):063001
- Norfleet DM, Sarosi PM, Manchiraju S, Wagner MF-X, Uchic MD, Anderson PM, Mills MJ (2009) Transformation-induced plasticity during pseudoelastic deformation in Ni–Ti microcrystals. Acta Mater 57(12):3549–3561
- Simon T, Kröger A, Somsen C, Dlouhy A, Eggeler G (2010) On the multiplication of dislocations during martensitic transformations in NiTi shape memory alloys. Acta Mater 58(5):1850–1860
- 11. Robertson SW, Pelton AR, Ritchie RO (2012) Mechanical fatigue and fracture of Nitinol. Int Mater Rev 57(1):1–36
- Pelton AR, Huang GH, Moine P, Sinclair R (2012) Effects of thermal cycling on microstructure and properties in Nitinol. Mater Sci Eng A 532:130–138
- Mahtabi MJ, Shamsaei N, Mitchell MR (2015) Fatigue of Nitinol: the state-of-the-art and ongoing challenges. J Mech Behav Biomed Mater 50:228–254
- Eggeler G, Hornbogen E, Yawny A, Heckmann A, Wagner M (2004) Structural and functional fatigue of NiTi shape memory alloys. Mater Sci Eng A 378:24–33
- Hornbogen E (2004) Review: Thermo-mechanical fatigue of shape memory alloys. J Mater Sci 39(2):385–399
- 16. Grossmann ch, Frenzel J, Sampath V, Depka T, Eggeler G (2009) Elementary transformation and deformation processes and the cyclic stability of NiTi and NiTiCu shape memory spring actuators. Metall Mater Trans A 40 A:2530–2544
- McKelvey AL, Ritchie RO (2001) Fatigue-crack growth behavior in the superelastic and shape-memory alloy Nitinol. Metall Mater Trans A 32(13):731–74
- Chluba C, Ge W, DeMiranda RL, Strobel J, Kienle L, Quandt E, Wuttig M (2015) Ultralow-fatigue shape memory alloy films. Science 348(6238):1004–1007
- Patoor E, Eberhardt A, Berveiller M (1996) Micromechanical modelling of superelasticity in shape memory alloys. Int J Plasticity 6(C1):277–292
- Patoor E, Lagoudas DC, Entchev PB, Brinson LC, Gao X (2006) Shape memory alloys. Part I: General properties and modeling of single crystals. Mech Mater 38:391–429
- Huang M, Gao X, Brinson LC (2000) A multivariant micromechanical model for SMAs Part 2. Polycrystal model. Int J Plasticity 16(10–11):1371–1390
- Gall K, Lim TJ, McDowell DL, Sehitoglu H, Chumlyakov YI (2000) The role of intergranular constraint on the stress-induced martensitic transformation in textured polycrystalline NiTi. Int J Plasticity 16(10–11):1189–1214
- Gao X, Huang M, Brinson LC (2000) A multivariant micromechanical model for SMAs Part 1. Crystallographic issues for single crystal model. Int J Plasticity 16(10–11):1345–1369
- Thamburaja P, Anand L (2001) Polycrystalline shape-memory materials: effect of crystallographic texture. J Mech Phys Solids 49(4):709–737
- Thamburaja P, Anand L (2002) Superelastic behavior in tensiontorsion of an initially-textured Ti-Ni shape-memory alloy. Int J Plasticity 18(11):1607–1617
- Anand L, Gurtin ME (2003) Thermal effects in the superelasticity of crystalline shape-memory materials. J Mech Phys Solids 51(6):1015–1058
- Thamburaja P (2005) Constitutive equations for martensitic reorientation and detwinning in shape-memory alloys. J Mech Phys Solids 53(4):825–856
- 28. Wang XM, Xu BX, Yue ZF (2008) Micromechanical modelling of the effect of plastic deformation on the mechanical behaviour



- in pseudoelastic shape memory alloys. Int J Plasticity 24(8):1307–1332
- Thamburaja P, Nikabdullah N (2009) A macroscopic constitutive model for shape-memory alloys: theory and finite-element simulations. Comput Methods Appl Mech Eng 198(9–12):1074–1086
- Manchiraju S, Anderson PM (2010) Coupling between martensitic phase transformations and plasticity: a microstructure-based finite element model. Int J Plasticity 26(10):1508–1526
- Yu C, Kang G, Kan Q, Zhu Y (2015) Rate-dependent cyclic deformation of super-elastic NiTi shape memory alloy: thermomechanical coupled and physical mechanism-based constitutive model. Int J Plasticity 72:60–90
- ASME (2006) ASME V&V 10–2006: guide for verification and validation in computational solid mechanics. American Society of Mechanical Engineers (ASME), New York
- ASME (2012) ASME V&V 10.1-2012: an illustration of the concepts of verification and validation in computational solid mechanics. American Society of Mechanical Engineers, New York
- Barber D (2012) Bayesian reasoning and machine learning.
 Cambridge University Press, Cambridge
- Santner TJ, Williams BJ, Notz W, Williams BJ (2003) The design and analysis of computer experiments, vol 1. Springer, Cham
- Kaipio J, Somersalo E (2006) Statistical and computational inverse problems, vol 160. Springer, Cham
- Stuart AM (2010) Inverse problems: a Bayesian perspective.
 Acta Numer 19:451–559
- 38. Smith RC (2013) Uncertainty quantification: theory, implementation, and applications, volume 12. SIAM, Philadelphia
- Gelman A, Carlin JB, Stern HS, Dunson DB, Vehtari A, Rubin DB (2013) Bayesian data analysis. CRC Press, Boca Raton
- Sullivan TJ (2015) Introduction to uncertainty quantification, vol 63. Springer, Cham
- Allmaras W, Bangerth M, Linhart JM, Polanco J, Wang F, Wang K, Webster J, Zedler S (2013) Estimating parameters in physical models through Bayesian inversion: a complete example. SIAM Rev 55(1):149–167
- Aguilar O, Allmaras M, Bangerth W, Tenorio L (2015) Statistics of parameter estimates: a concrete example. SIAM Rev 57(1):131–149
- Tarantola Albert (2005) Inverse problem theory and methods for model parameter estimation. SIAM, Philadelphia
- Kennedy MC, O'Hagan A (2001) Bayesian calibration of computer models. J R Stat Soc Ser B Stat Methodol 63(3):425–464
- 45. Collis J, Connor AJ, Paczkowski M, Kannan P, Pitt-Francis J, Byrne HM, Hubbard ME (2017) Bayesian calibration, validation and uncertainty quantification for predictive modelling of tumour growth: a tutorial. Bull Math Biol 79(4):939–974
- Wu X, Kozlowski T, Meidani H, Shirvan K (2018) Inverse uncertainty quantification using the modular Bayesian approach based on Gaussian process, Part 1: theory. Nucl Eng Des 335:339–355
- 47. Strong M, Oakley JE (2014) When is a model good enough? Deriving the expected value of model improvement via specifying internal model discrepancies. SIAM/ASA J Uncertainty Quant 2(1):106–125
- 48. Sargsyan K, Najm HN, Ghanem R (2015) On the statistical calibration of physical models. Int J Chem Kinet 47(4):246–276
- He Y, Xiu D (2016) Numerical strategy for model correction using physical constraints. J Comput Phys 313:617–634
- Rizzi F, Khalil M, Jones RE, Templeton JA, Ostien JT, Boyce BL (2019) Bayesian modeling of inconsistent plastic response

- due to material variability. Comput Methods Appl Mech Eng 353:183-200
- Geyer CJ (1992) Practical Markov Chain Monte Carlo. Stat Sci 7(4):473–483
- Andrieu C, Freitas ND, Doucet A, Jordan MI (2003) An introduction to MCMC for machine learning. Mach Learn 50(1–2):5–43
- 53. Metropolis N, Ulam S (1949) The Monte Carlo method. J Am Stat Assoc 44(247):335–341
- Hastings WK (1970) Monte Carlo sampling methods using Markov chains and their applications. Biometrika 57(1):97–109
- Andrieu C, Thoms J (2008) A tutorial on adaptive MCMC. Stat Comput 18(4):343–373
- Bray JH, Maxwell SE (1985) Multivariate analysis of variance, vol 54. SAGE, Thousand Oaks
- 57. Weinfurt KP (1995) Multivariate analysis of variance. In: The SAGE encyclopedia of communication research methods. SAGE, Thousand Oaks
- Scheffe H (1999) The analysis of variance, vol 72. Wiley, New York
- Murray-Smith DJ (2012) Modelling and simulation of integrated systems in engineering: issues of methodology, quality, testing and application. Elsevier, Amsterdam
- Honarmandi P, Duong TC, Ghoreishi SF, Allaire D, Arroyave R (2019) Bayesian uncertainty quantification and information fusion in Calphad-based thermodynamic modeling. Acta Mater 164:636–647
- Honarmandi P, Paulson NH, Arróyave R, Stan M (2019) Uncertainty quantification and propagation in Calphad modeling. Model Simul Mater Sci Eng 27(3):034003
- Honarmandi P, Arróyave R (2020) Uncertainty quantification and propagation in computational materials science and simulation-assisted materials design. Integr Mater Manuf Innov 9:103–143
- Wasserman L et al (2000) Bayesian model selection and model averaging. J Math Psychol 44(1):92–107
- 64. Chipman H, George EI, McCulloch RE, Clyde M, Foster DP, Stine RA (2001) The practical implementation of Bayesian model selection. Lecture notes monograph series, pp 65–134. Institute of Mathematical Statistics, Hayward
- Ando T (2010) Bayesian model selection and statistical modeling. CRC Press, Boca Raton
- Gall K, Dunn ML, Liu Y, Labossiere P, Sehitoglu H, Chumlyakov YI (2002) Micro and macro deformation of single crystal NiTi. J Eng Mater Technol 124(2):238–245
- Hane KF, Shield TW (1999) Microstructure in the cubic to monoclinic transition in titanium-nickel shape memory alloys. Acta Mater 47(9):2603–2617
- Chumlyakov YI, Kireeva IV, Korotaev AD, Litvinova EI, Zuev YL (1996) Mechanisms of plastic deformation, hardening, and fracture in single crystals of nitrogen-containing austenitic stainless steels. Russ Phys J 39(3):189–210
- Ezaz T, Wang J, Sehitoglu H, Maier HJ (2013) Plastic deformation of NiTi shape memory alloys. Acta Mater 61(1):67–78
- Miyazaki S, Imai T, Igo Y, Otsuka K (1986) Effect of cyclic deformation on the pseudoelasticity characteristics of Ti-Ni alloys. Metall Trans A 17(1):115–120
- Eggeler G, Hornbogen E, Yawny A, Heckmann A, Wagner M (2004) Structural and functional fatigue of NiTi shape memory alloys. Mater Sci Eng A 378(1):24–33
- 72. Yawny A, Sade M, Eggeler G (2005) Pseudoelastic cycling of ultra-fine-grained NiTi shape-memory wires. Z Metall 96(6):608–618
- Nemat-Nasser S, Guo WG (2006) Superelastic and cyclic response of NiTi SMA at various strain rates and temperatures. Mech Mater 38(5–6):463–474



- Zaki W, Moumni Z (2007) A 3D model of the cyclic thermomechanical behavior of shape memory alloys. J Mech Phys Solids 55(11):2427–2454
- Kang G, Kan Q, Qian L, Liu Y (2009) Ratchetting deformation of super-elastic and shape-memory NiTi alloys. Mech Mater 41(2):139–153
- Kang G, Kan Q, Yu C, Song D, Liu Y (2012) Whole-life transformation ratchetting and fatigue of super-elastic NiTi Alloy under uniaxial stress-controlled cyclic loading. Mater Sci Eng A 535:228–234
- Delville R, Kasinathan S, Zhang Z, Humbeeck JV, James RD, Schryvers D (2010) Transmission electron microscopy study of phase compatibility in low hysteresis shape memory alloys. Philos Mag 90(1–4):177–195
- Manchiraju S, Gaydosh D, Benafan O, Noebe R, Vaidyanathan R, Anderson PM (2011) Thermal cycling and isothermal deformation response of polycrystalline NiTi: simulations vs. experiment. Acta Mater 59(13):5238–5249
- Delville R, Malard B, Pilch J, Sittner P, Schryvers D (2011)
 Transmission electron microscopy investigation of dislocation slip during superelastic cycling of Ni–Ti wires. Int J Plasticity 27(2):282–297
- Morin C, Moumni Z, Zaki W (2011) A constitutive model for shape memory alloys accounting for thermomechanical coupling. Int J Plasticity 27(5):748–767
- Morin C, Moumni Z, Zaki W (2011) Thermomechanical coupling in shape memory alloys under cyclic loadings: experimental analysis and constitutive modeling. Int J Plasticity 27(12):1959–1980
- Sun L, Huang WM, Ding Z, Zhao Y, Wang CC, Purnawali H, Tang C (2012) Stimulus-responsive shape memory materials: a review. Mater Des 33:577–640
- Yin H, Sun Q (2012) Temperature variation in NiTi shape memory alloy during cyclic phase transition. J Mater Eng Perform 21(12):2505–2508
- 84. Yin H, He Y, Sun Q (2014) Effect of deformation frequency on temperature and stress oscillations in cyclic phase transition of NiTi shape memory alloy. J Mech Phys Solids 67:100–128
- Song D, Kang G, Kan Q, Yu C, Zhang C (2014) Non-proportional multiaxial transformation ratchetting of super-elastic NiTi shape memory alloy: experimental observations. Mech Mater 70:94–105
- 86. Benafan O, Noebe RD, Padula SA II, Brown DW, Vogel S, Vaidyanathan R (2014) Thermomechanical cycling of a NiTi shape memory alloy-macroscopic response and microstructural evolution. Int J Plasticity 56:99–118
- Otsuka K, Ren X (2005) Physical metallurgy of Ti-Ni-based shape memory alloys. Prog Mater Sci 50(5):511–678
- Hossain A, Baxevanis T (2021) A finite strain thermomechanically-coupled constitutive model for phase transformation and (transformation-induced) plastic deformation in NiTi single crystals. Int J Plasticity. https://doi.org/10.1016/j.ijplas.2021. 102957
- Cherkaoui M, Berveiller M, Sabar H (1998) Micromechanical modeling of martensitic transformation induced plasticity (TRIP) in austenitic single crystals. Int J Plasticity 14(7):597–626
- Yu C, Kang G, Kan Q (2015) A micromechanical constitutive model for anisotropic cyclic deformation of super-elastic NiTi

- shape memory alloy single crystals. J Mech Phys Solids 82:97–136
- Monroe JA, Gehring D, Karaman I, Arroyave R, Brown DW, Clausen B (2016) Tailored thermal expansion alloys. Acta Mater 102:333–341
- Yu C, Kang G, Sun Q, Fang D (2019) Modeling the martensite reorientation and resulting zero/negative thermal expansion of shape memory alloys. J Mech Phys Solids 127:295–331
- Wagner MF-X, Windl W (2008) Lattice stability, elastic constants and macroscopic moduli of NiTi martensites from first principles. Acta Mater 56(20):6232–6245
- 94. Coleman BD. and Noll W. (1974) The thermodynamics of elastic materials with heat conduction and viscosity. In: The foundations of mechanics and thermodynamics. Springer, Berlin, pp 145–156
- 95. Peirce D, Fong Shih C, Needleman A (1984) A tangent modulus method for rate dependent solids. Comput Struct 18(5):875–887
- 96. Cormeau I (1975) Numerical stability in quasi-static elasto/visco-plasticity. Int J Numer Methods Eng 9(1):109–127
- Gelfand AE, Diggle P, Guttorp P, Fuentes M (2010) Handbook of spatial statistics. CRC Press, Boca Raton
- Martins TG, Simpson DP, Riebler A, Rue H, Sørbye SH (2014)
 Penalising model component complexity: a principled, practical approach to constructing priors. arXiv preprint. arXiv:1403.4630
- Haario H, Saksman E, Tamminen J et al (2001) An adaptive metropolis algorithm. Bernoulli 7(2):223–242
- 100. Jeffreys H (1935) Some tests of significance, treated by the theory of probability. In: Mathematical proceedings of the Cambridge philosophical society, vol 31. Cambridge University Press, Cambridge, pp 203–222
- Kass RE, Raftery AE (1995) Bayes factors. J Am Stat Asso 90(430):773–795
- Montgomery DC (2017) Design and analysis of experiments.
 Wiley, New York
- 103. Honarmandi P, Solomou A, Arroyave R, Lagoudas D (2019) Uncertainty quantification of the parameters and predictions of a phenomenological constitutive model for thermally induced phase transformation in Ni–Ti shape memory alloys. Model Simul Mater Sci Eng 27(3):034001
- 104. Brill TM, Mittelbach S, Assmus W, Mullner M, Luthi B (1991) Elastic properties of NiTi. J Phys Condens Matter 3(48):9621
- Matsumoto O, Miyazaki S, Otsuka K, Tamura H (1987) Crystallography of martensitic transformation in Ti-Ni single crystals. Acta Metall 35(8):2137–2144
- 106. Gall K, Sehitoglu H (1999) The role of texture in tensioncompression asymmetry in polycrystalline NiTi. Int J Plasticity 15(1):69–92
- 107. Siredey N, Patoor E, Berveiller M, Eberhardt A (1999) Constitutive equations for polycrystalline thermoelastic shape memory alloys: Part I. Intragranular interactions and behavior of the grain. Int J Solids Struc 36(28):4289–4315
- 108. Beyerlein IJ, Tomé CN (2008) A dislocation-based constitutive law for pure Zr including temperature effects. Int J Plasticity 24(5):867–895

Publisher's Note Springer Nature remains neutral with regard to jurisdictional claims in published maps and institutional affiliations.

